The Astrophysical Journal, 934:161 (11pp), 2022 August 1 https://doi.org/10.3847/1538-4357/ac7a44

Constraining Global Solar Models through Helioseismic Analysis

Andrey M. Stejko[1], Alexander G. Kosovichev[1], Nicholas A. Featherstone[2], Gustavo Guerrero[1,3], Bradley W. Hindman[4,5], Loren I. Matilsky[4,5], and Jörn Warnecke[6]
[1] New Jersey Institute of Technology, Newark, NJ 07012, USA; ams226@njit.edu
[2] SWRI, Department of Space Studies, Boulder, CO 80302, USA
[3] Universidade Federal de Minas Gerais, Belo Horizonte, MG, 31270-901, Brazil
[4] JILA, University of Colorado, Boulder, CO 80309-0440, USA
[5] Applied Mathematics, University of Colorado, Boulder, CO 80309-0526, USA
[6] Max-Planck-Institut für Sonnensystemforschung, Justus-von-Liebig-Weg 3, D-37077 Göttingen, Germany
Received 2022 April 8; revised 2022 June 12; accepted 2022 June 16; published 2022 August 3

Abstract

Global hydrodynamic simulations of internal solar dynamics have focused on replicating the conditions for solar-like (equator rotating faster than the poles) differential rotation and meridional circulation using the results of helioseismic inversions as a constraint. Inferences of meridional circulation, however, have provided controversial results showing the possibility of one, two, or multiple cells along the radius. To help address this controversy and develop a more robust understanding of global flow regimes in the solar interior, we apply a "forward-modeling" approach to the analysis of helioseismic signatures of meridional circulation profiles obtained from numerical simulations. We employ the global acoustic modeling code GALE to simulate the propagation of acoustic waves through regimes of mean mass-flows generated by global hydrodynamic and magnetohydrodynamic models: EULAG, the Pencil code, and the Rayleigh code. These models are used to create synthetic Dopplergram data products, used as inputs for local time–distance helioseismology techniques. Helioseismic travel-time signals from solutions obtained through global numerical simulations are compared directly with inferences from solar observations, in order to set additional constraints on global model parameters in a direct way. We show that even though these models are able to replicate solar-like differential rotation, the resulting rotationally constrained convection develops a multicell global meridional circulation profile that is measurably inconsistent with local time–distance inferences of solar observations. However, we find that the development of rotationally unconstrained convection close to the model surface is able to maintain solar-like differential rotation, while having a significant impact on the helioseismic travel-time signal, replicating solar observations within one standard deviation of the error due to noise.

Unified Astronomy Thesaurus concepts: Helioseismology (709); Solar convective zone (1998); Solar meridional circulation (1874); Hydrodynamical simulations (767)

1. Introduction

The implementation of nonlinear hydrodynamic (HD) and magnetohydrodynamic (MHD) modeling is often contrasted with mean-field simulations, which have found success in replicating solar processes and building out models of the global dynamics that drive solar mean mass-flows (Ruediger 1989; Kitchatinov & Ruediger 1995; Kitchatinov 2004; Pipin & Kosovichev 2018) and the generation of the global solar dynamo—see Charbonneau (2020) for a comprehensive review. These models, however, often require ad hoc prescriptions of internal solar parameters, resulting in potentially unrealistic distributions and amplitudes of turbulent transport coefficients, along with as of yet unknown mechanisms that may have significant impacts on mean mass-flows. Nonlinear HD/MHD modeling attempts to replicate global solar flows through a more holistic development of global dynamics and the solar dynamo, by simulating convective energy transport in simplified models of solar plasma. Nonlinear global modeling, in particular, has made tremendous strides since the seminal works of Gilman (1972) and Gilman & Miller (1981). This can be seen most clearly in simulations analyzing the conditions for solar-like differential rotation (e.g., Guerrero et al. 2013; Gastine et al. 2014; Fan & Fang 2014; Featherstone & Miesch 2015; Matilsky et al. 2019, 2020; Warnecke & Käpylä 2020; Hotta et al. 2022).

In-depth investigations have been made possible due in part to the success of global helioseismology in mapping the rotational structure of the solar interior (e.g., Kosovichev et al. 1997; Schou et al. 1998, 2002; Howe et al. 2011) providing detailed constraints for solar models to replicate. Reliably inferring the Sun's internal meridional circulation, however, has remained a difficult problem. Local time–distance helioseismology techniques have had significantly more trouble probing into deeper parts of the solar convection zone ($r < 0.96R_\odot$). Large-scale systematic errors such as the center-to-limb (CToL) effect (see Zhao et al. 2012; Chen 2019), and apparent downflows in magnetic regions (Liang & Chou 2015), have proven challenging to disentangle effectively—resulting in widely varying conjectures on the structure of meridional circulation in the solar convection zone (SCZ). This has culminated in a disagreement over whether meridional circulation exhibits a single-cell (Gizon et al. 2020) or a double-/multicell structure (Zhao et al. 2013; Kholikov et al. 2014; Chen 2019). Progress has steadily been made, however, with the development of new approaches to disentangling the

CToL effect using frequency-dependent analysis (Chen 2019; Rajaguru & Antia 2020).

Recent helioseismic analysis of synthetic Dopplergram data generated by global acoustic models has shown that the noise in time–distance measurements is too high to make pronouncements on whether meridional circulation has more than one cell (Stejko et al. 2021b). Helioseismic observations, however, can still be useful in setting constraints on global, nonlinear, convectively driven models in a limited capacity. Even though differentiating between single-cell and multicell structures remains difficult, we can gauge how well the particular multicell structure commonly exhibited by MHD/HD models in solar-like rotational regimes (e.g., Guerrero et al. 2013; Käpylä et al. 2013; Featherstone & Miesch 2015; Matilsky et al. 2019; Hindman et al. 2020; Warnecke & Käpylä 2020) agrees with solar observations, and what critical insights can be gained from global models of turbulent solar convection. We apply a "forward-modeling" method to compare helioseismic travel-time signatures of these models directly to solar observations (Stejko et al. 2021a, 2021b)—computing travel-time differences using local time–distance helioseismic techniques on synthetic Dopplergram data. These data are created using a global acoustic code that computes oscillations over background velocities imported from nonlinear convectively driven models. Comparing the resulting travel-time differences to those taken from observational full-disk Dopplergram data results in a more direct comparison of measured signals without relying on inversions to estimate velocity profiles.

This paper is organized as follows. In Section 2 we briefly describe the computational setup of the acoustic simulation code and time–distance helioseismic analysis procedure, used to generate and analyze synthetic Dopplergrams. In Section 3 we present results of helioseismic measurements for convectively driven models R1x, M5, and H38 (described therein), and in Section 4 we analyze the helioseismic signatures generated by models with a varying stratification (N3 and N5). Section 5 presents a comparison of results with solar observations, and finally, in Section 6 we offer an analysis and discussion of how these results can be employed as constraints on the future development of global convectively driven solar models.

2. Acoustic Modeling and Helioseismic Analysis

A compressible 3D acoustic simulation code (GALE; Stejko et al. 2021a) is used to generate synthetic Dopplergrams for the forward-modeling analysis of convectively driven hydrodynamic global models. This algorithm employs novel pseudospectral methods to offer an efficient and flexible platform for computing the contributions of 3D background flow structures to acoustic perturbations within the simulated solar interior. The Euler equations are solved in their conservative form, in a fully spherical domain: $0 < \theta < \pi$, $0 < \phi \leqslant 2\pi$, $0 < r \leqslant 1.001 R_\odot$.

$$\frac{\partial \rho'}{\partial t} + \Upsilon' = 0, \tag{1}$$

$$\frac{\partial \Upsilon'}{\partial t} + \mathcal{M}' = -\nabla^2(p') - \nabla \cdot (\rho' \tilde{g}_r \hat{\mathrm{r}}) + \nabla \cdot S\hat{\mathrm{r}}, \tag{2}$$

$$\frac{\partial p'}{\partial t} = -\frac{\Gamma_1 \tilde{p}}{\tilde{\rho}} \left(\mathcal{O}_p + \tilde{\rho} \boldsymbol{u}' \cdot \frac{N^2}{g} \hat{r} \right). \tag{3}$$

Linear perturbations in the potential field are computed, with solenoidal contributions discarded. This is achieved with a split-field formulation, by computing the divergence of the momentum field ($\Upsilon = \nabla \cdot \rho \boldsymbol{u}$). The governing equations are then linearized by solving for perturbations (denoted by a prime) from base parameters (denoted by a tilde) of pressure (p), density (ρ), gravity (g), the Brunt–Väisälä frequency (N^2), and the adiabatic ratio (Γ_1). Contributions of the divergence of the material derivative are denoted by $\mathcal{M}'$, and adiabatic contributions to the conservation of energy are denoted by $\mathcal{O}_p$. 3D solar oscillation data are generated for user-specified background flow profiles ($\tilde{\boldsymbol{u}}$), reproducing shifts to the solar oscillation spectrum (Stejko et al. 2021a). This algorithm is optimized for massively parallel computing with a hybrid implementation of distributed-memory processing using the Message Passing Interface (MPI), alongside the shared-memory Open Multi-Processing (OpenMP) protocol. The pseudospectral computational method works by decomposing field terms into vector spherical harmonic (VSH) and tensor spherical harmonic (TSH) bases (see Stejko et al. 2021a), allowing for the efficient computation of symmetric second-order tensor and dyad terms. Realization noise, mimicking the kind seen in observational data, is simulated through a stochastic excitation of source terms (S) generated by a chi-squared distribution of random frequency perturbations in the top 0.1% of the solar interior.

We create synthetic Dopplergrams using global 3D background velocity profiles generated by the nonlinear convection simulations of the solar interior performed with the EULAG code, the Rayleigh code, and the Pencil code, each producing slightly different regimes of meridional circulation. In order to characterize and compare the helioseismic effects of each of these regimes, as opposed to the effect of any azimuthal idiosyncrasies, we compute the toroidal average of the meridional circulation profiles, using azimuthally symmetric velocities as inputs for background velocity terms ($\tilde{u}_r$, $\tilde{u}_\theta$). The GALE code is initialized to a maximum spectral resolution of $\ell_{\max} = 200$—high enough to sample the convective interior up to $r \sim 0.96 R_\odot$. The acoustic wave-field is evolved for approximately 67 hr of model time, generating synthetic Dopplergram data sampled from the model approximately 300 km above the solar surface ($R_\odot = 6.9599 \times 10^{10}$ cm). Such a timescale is too short to effectively resolve the travel-time signal from realization noise (Braun & Birch 2008), so we leverage the dependence of the signal-to-noise ratio on the square root of the temporal sampling window, increasing background velocities by a factor of 25 (Hartlep et al. 2013), effectively simulating approximately 5 yr of observations.

To analyze the resulting synthetic Dopplergram data, we employ the local time–distance helioseismology technique described by Zhao et al. (2009) and Stejko et al. (2021b). This method allows global mean flows in the solar interior to be inferred by measuring their impact on the acoustic wave-field. Waves traveling in opposite directions along p-mode ray paths will exhibit travel-time differences when moving through a medium with some average velocity along their path. These travel-time differences are calculated from a cross correlation of two points on the solar surface, through the process of Gabor wavelet fitting (Kosovichev & Duvall 1997), where a wave-packet function (see Stejko et al. 2021a) is fit to the measured signal using the iterative Levenberg–Marquardt method. Each pixel in the synthetic Dopplergram, between a latitude range of

50°N and 50°S, is treated as the center of a 60° × 60° patch that is remapped into an azimuthal equidistant projection (Postel's projection) at a resolution of approximately 0.6° per pixel. The radius of concentric circles drawn on this patch represents half of the angular distance along the model surface (Δ) that the acoustic ray travels, penetrating a maximum depth (r_i) at the center of the patch that can be estimated as $r_i = c(r_i)L/\omega$, where c is the sound speed, ω is the angular frequency, and $L = \sqrt{l(l+1)}$ is effectively the spherical harmonic degree. Pixels are selected along these circles at every interval (1°.2) for 12°–42°, corresponding to an approximate depth of $r_i = 0.93R_\odot - 0.72R_\odot$. 30°-wide sectors in the north and south (1 pixel in radius) are then averaged, cross-correlated, and smoothed (using the procedure described by Stejko et al. 2021b), in order to compute the travel-time differences created by mean meridional flows in the global model. These travel-time differences can then be used to estimate the depth dependence of velocity contributions (Birch & Kosovichev 2001). In this analysis, however, we compare travel-time measurements obtained from global convection simulations directly to those computed from solar observations (Section 4), without the need to rely on approximations made using inversion techniques.

3. Analyzing Meridional Profiles of Convectively Driven Models

We compare three meridional profiles generated by the nonlinear convectively driven HD/MHD codes: EULAG (Smolarkiewicz & Charbonneau 2013), the Pencil code (Käpylä et al. 2012; Warnecke 2018; Warnecke & Käpylä 2020; Pencil Code Collaboration et al. 2021), and the Rayleigh code (Featherstone & Hindman 2016; Featherstone et al. 2021). The first meridional circulation profile that we analyze is described as model R1x by G. Guerrero et al. (2022, in preparation), generated using the hydrodynamic (without the magnetic field) global model EULAG, where the anelastic approximation is used to simulate convection in a global computational domain measuring $0 \leqslant \phi \leqslant 2\pi$, $0 \leqslant \theta \leqslant \pi$, and $0.60R_\odot \leqslant r \leqslant 0.964R_\odot$. In this model, convection is primarily driven by a superadiabatic state, prescribed with an ambient potential temperature function for an ideal gas, whose polytropic index corresponds to marginally unstable convection ($m < 1.5$). The index is chosen to mimic the density stratification prescribed by the solar model S (Christensen-Dalsgaard et al. 1996) within the computational domain—corresponding to approximately $N_\rho = 3.64$ density scale heights in the simulated convection zone ($r = 0.70R_\odot - 0.964R_\odot$). The angular rotation rate of the reference frame is set to slightly above the average solar rotation rate ($\Omega_0 = 1.06\Omega_\odot$, where $\Omega_\odot = 2.87 \times 10^{-6}\,\mathrm{s}^{-1}$), sufficient to maintain solar-like differential rotation, at a global Rossby number of $\mathrm{Ro} = 0.56$ in the convection zone (with a radial extent of $H = 0.964R_\odot - 0.72R_\odot$), calculated as $\mathrm{Ro} = (2\Omega_0\tau_c)^{-1}$, where $\tau_c = H/u_{\mathrm{rms}}$ is the convective turnover time. The resulting meridional circulation profile can be seen in panel (a) of Figure 1.

The Pencil code (Pencil Code Collaboration et al. 2021) is a high-order finite-difference algorithm used for the computation of compressible magnetohydrodynamics on highly parallelized computational architectures. The full code and instructions for its use and installation are maintained on https://github.com/pencil-code/pencil-code. This code has been employed for global dynamo simulations in a wedge geometry represented by a quarter-spherical mesh grid measuring $0 \leqslant \phi \leqslant \pi/2$, $\pi/12 < \theta < 11\pi/12$, and $0.70R_\odot < r \leqslant R_\odot$. The computational setup is described in detail by Käpylä et al. (2013). This algorithm is used to simulate the development of the global solar dynamo by simulating heat flux ($\partial T/\partial r$) at the bottom boundary and prescribing a radiative heat conductivity profile that falls off with increased radius ($K \sim r^{-15}$). This model has been used to investigate the rotational dependence of global solar properties (e.g., Warnecke 2018; Warnecke & Käpylä 2020), evincing solar-like differential rotation at higher rotation rates—represented by a Rossby number of $\mathrm{Ro} < 0.27$, where $\mathrm{Ro} = (2\Omega_0\tau_c)^{-1}$ and τ_c is defined as the convective turnover time, averaged over the entire computational domain. We analyze model M5 (Warnecke & Käpylä 2020) with an angular rotation rate of $\Omega_0 = 4.7\Omega_\odot$ ($\Omega_0 = 5\Omega_\odot$ in their paper, where $\Omega_\odot = 2.7 \times 10^{-6}\,\mathrm{s}^{-1}$) and a Rossby number of $\mathrm{Ro} < 0.12$. This model is actuated with a large-scale magnetic field, influencing the development of meridional flow. The resulting meridional circulation profile can be seen in panel (b) of Figure 1.

Rayleigh is a highly parallelized pseudospectral algorithm used to simulate convection in stellar interiors under the anelastic approximation (see Featherstone & Hindman 2016, for details). The full code, as well as its instructions for use and installation, are made freely available at https://github.com/geodynamics/Rayleigh and through Featherstone et al. (2021). Background states are represented by the adiabatic stratification of an ideal gas with a polytropic index of $n = 1.5$, defined as a function of density scale heights throughout the domain (N_ρ). The number of scale heights can be freely altered to simulate various stratification regimes, with $N_\rho = 3$ most closely resembling the density profile in the solar model S (Christensen-Dalsgaard et al. 1996) inside the simulated radial range ($0.718R_\odot \leqslant r \leqslant 0.946R_\odot$). Convection is driven by a constant deposition of energy into the domain, with a linear radial dependence on internal pressure. The dispersal of this energy occurs via heat conduction at the upper boundary, set by the stellar luminosity parameter L_*. Models are computed on a fully spherical shell ($0 \leqslant \phi \leqslant 2\pi$, $0 < \theta < \pi$, $0.718R_\odot \leqslant r \leqslant 0.946R_\odot$). The meridional circulation profile for model H38 (Hindman et al. 2020) can be seen in panel (c) of Figure 1. This model is characterized by three density scale heights ($N_\rho = 3$), a rotation rate of $\Omega_0 = 2\Omega_\odot$ (where $\Omega_\odot = 2.87 \times 10^{-6}\,\mathrm{s}^{-1}$), a bulk flux Rayleigh number of $\mathrm{Ra} = 8.61 \times 10^5$ (see Hindman et al. 2020 for details), and a Rossby number of $\mathrm{Ro} = 5.94 \times 10^{-2}$—exhibiting a solar-like differential rotation at the edge of antisolar (equator rotating slower than poles) transition, as well as a multicell arrangement of its meridional circulation profile. The Rossby number in their paper is calculated as $\mathrm{Ro} = u_{\mathrm{rms}}(2\Omega_0 H)^{-1}$, where u_{rms} is the rms velocity integrated over the full spherical shell, with radial size H.

Models R1x and H38 are stretched in order to match the radial extent of the solar surface ($r = R_\odot$), with the size of each radial mesh-point multiplied by a constant value. The global flow profiles are then used as background velocity terms in our linearized model, whose stratification is described by the solar model S (Christensen-Dalsgaard et al. 1996). This creates a small discrepancy between the stratification that was used to generate the flows and our simulation; however, this is not a significant concern as these models do not purport to faithfully replicate turbulent convective parameters on the Sun, and the

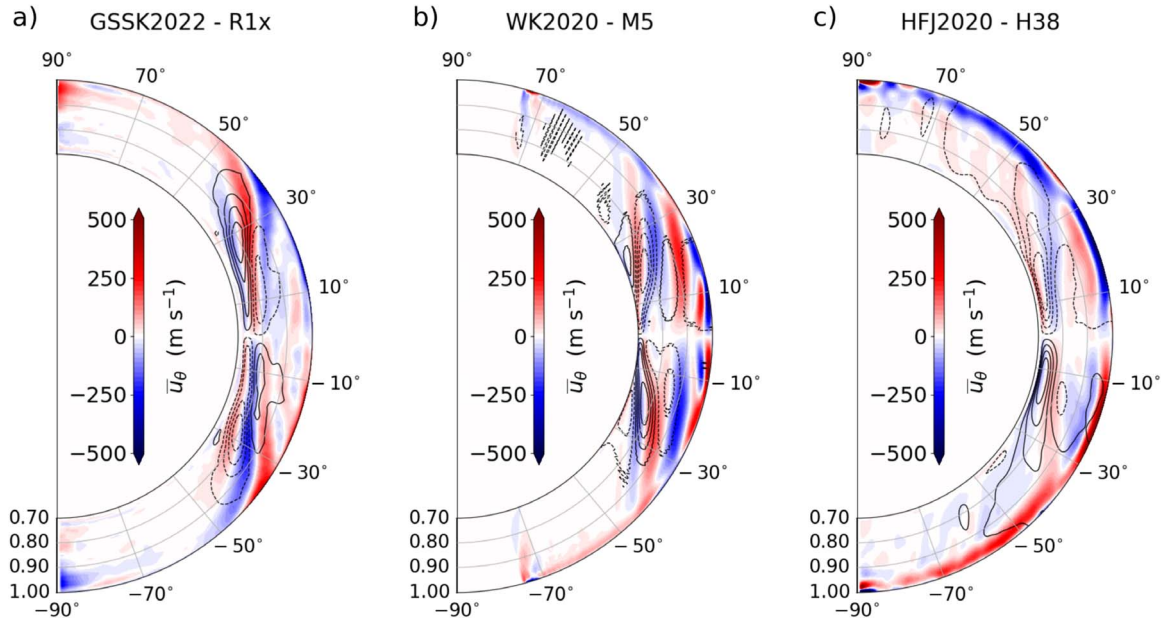

Figure 1. Latitudinal velocities ($\tilde{u}_\theta$) amplified to a maximum of 500 m s^{-1}. Meridional circulation profiles are shown corresponding to a solar-like differential rotation generated by convectively driven models of (a) EULAG (G. Guerrero et al. 2022, in preparation), (b) the Pencil code (Warnecke & Käpylä, 2020), and (c) the Rayleigh code (Hindman et al. 2020). Solid and dashed contours represent counterclockwise and clockwise circulation, respectively, with positive (negative) values depicting a southward (northward) flow.

resulting global flow profiles are still unable to completely reproduce solar dynamics. Stretching these profiles, however, allows for a better interpretation of the helioseismic signals that these simulated regimes would generate if they reached the surface—giving us a better idea of the constraints that can be placed on such models with time–distance helioseismology. Furthermore, these models are unable to replicate the high levels of stratification near the solar surface, as well as their corresponding flow dynamics; as such, we limit our time–distance analysis to deeper into the model interior ($r < 0.93R_\odot$), where the impact of these flows on the signal is significantly reduced. Meridional velocities (u_r, u_θ) of the model profiles are amplified to a maximum of 500 m s^{-1}—a 25-fold increase in surface velocity—peaking at a maximum of $\sim$20 m s^{-1} and averaging out to $\sim$10–17 m s^{-1} in regions of interest on the model surface (cf. Roudier et al. 2018).

The meridional circulation profiles are characterized by Taylor columns strongly aligned with the rotational axis, indicative of the models' inability to break the Taylor–Proudman balance (Ruediger 1989; Kitchatinov & Ruediger 1995; Rempel 2005) in fast-rotating regimes. These low-latitude columnar cells correspond to cylindrical convective modes, known as banana cells or Busse columns (Busse 1970), that are seen to develop in convectively driven solar and stellar simulations (e.g., Käpylä et al. 2011; Guerrero et al. 2013; Featherstone & Miesch 2015; Hindman et al. 2020). A prominent feature of such models is shown in their inability to develop strong continuous circulation cells that stretch across the latitudinal extent such as those inferred in solar observations of subsurface meridional circulation (Zhao et al. 2013; Schad et al. 2013; Kholikov et al. 2014; Lin & Chou 2018; Gizon et al. 2020). This is true of models R1x and M5, as well as other solar-like differential rotation models generated by the Rayleigh code (see Hindman et al. 2020). Model H38 appears to deviate from this trend, however, showing mostly continuous poleward flows with a small exception around the 45° latitude—a potential result of the limited rotational constraint (especially near the surface) on the model. Another feature commonly observed in these models is the formation of multiple cells with return flows very close to the model surface, with many managing to break through to the upper boundary. This has a very noticeable effect on the helioseismic signature that can be visualized by plotting N–S travel-time differences ($\delta\tau_{\rm NS}$) as a function of their travel distance ($\Delta = 12°$–$42°$)—corresponding to turning points: $r = 0.93R_\odot - 0.72R_\odot$, respectively, in the solar interior. In order to reduce noise in our measurements, we plot latitudinal averages of these travel-time differences in places that approximately correspond with similar continuous features seen in the models, expressed by the five following ranges: 30° N–50°N, 10°N–30°N, 10°S–10°N, 10°S–30°S, and 30°S–50° S. The travel-time differences for the three regimes of meridional circulation (R1x, M5, and H38) can be seen in Figure 2, where travel-time differences sampled from our synthetic Dopplergram data are shown as solid lines, and are compared with the expected travel-time differences computed using the ray-path approximation (Equation (4); Giles 2000), shown as dashed lines—estimating travel-time shifts from velocity contributions along the unperturbed acoustic ray path (Γ_0):

$$\delta\tau = -2\int_{\Gamma_0} \frac{\boldsymbol{u}\cdot\boldsymbol{n}}{c^2}\, ds. \tag{4}$$

The integral is computed by tracing p-mode ray paths through the 3D profiles of background velocities taken from models R1x, M5, and H38, using Simpson's rule to numerically integrate the velocity in each mesh-point that the ray intersects. Even though only linear contributions of the background velocities in the model interior are considered, we can see in Figure 2 that this approximation is mostly within the error range of one standard deviation of the noise—setting a baseline target for the accuracy of our time–distance analysis method to

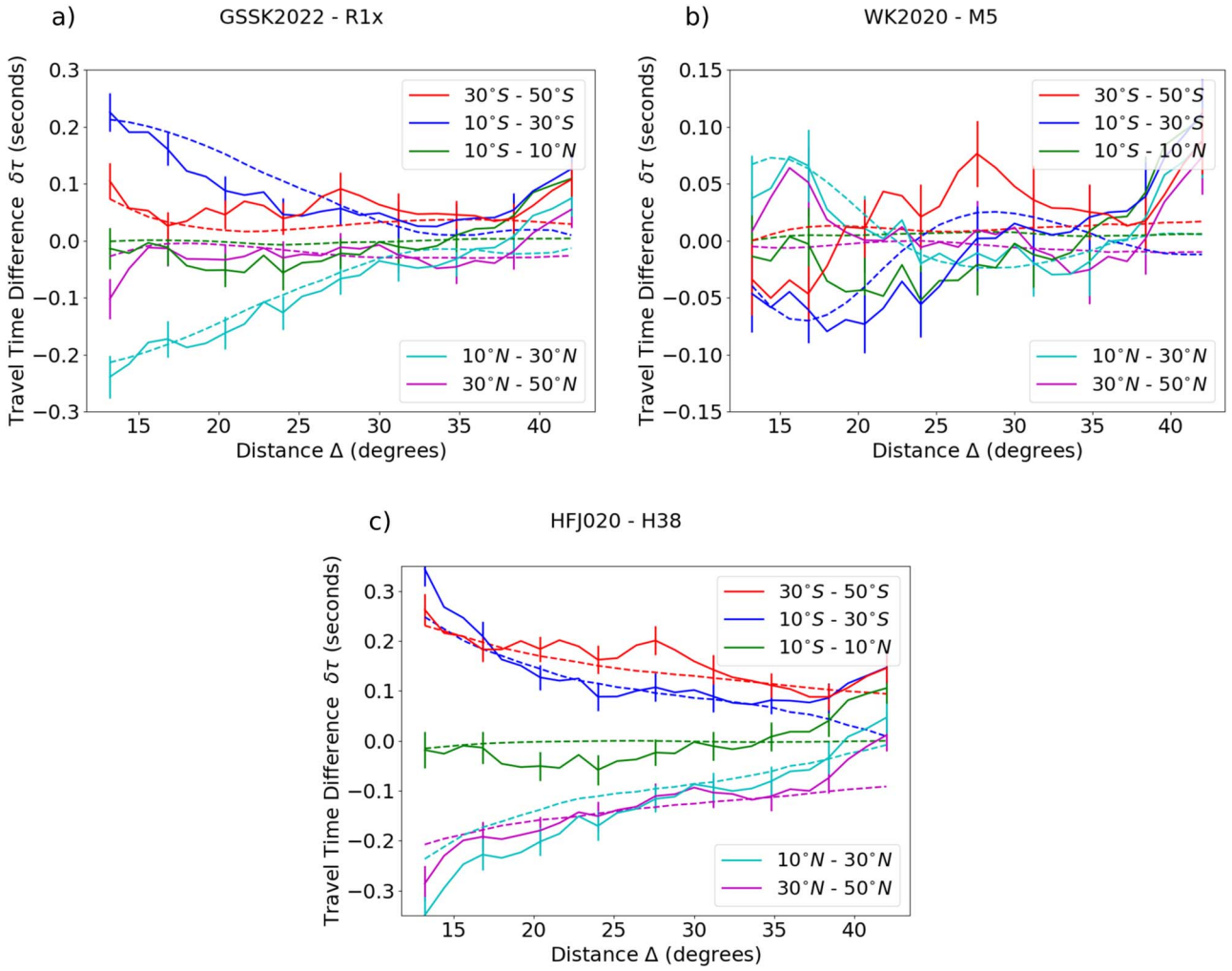

Figure 2. The N–S travel-time differences ($\delta\tau_{\rm NS}$) as a function of travel distance (Δ) for models R1x (a), M5 (b), and H38 (c). The travel-time measurements are phase-speed filtered ($\sigma = 0.05v_p$; Nigam et al. 2007) and shown as solid lines for five latitudinal averages. Dashed lines are theoretical times computed using the ray-path approximation (Equation (4); Giles 2000). Error bars show the standard deviation of the measured noise ($\sigma_{\rm NS}$; Equation (5)).

the known velocities in the model interior. The travel-time differences are divided by the same factor of 25 that velocity values (u_r, u_θ) were amplified by—justified by their close match to the linear ray-path approximation (seen in Figure 3). Error bars represent one standard deviation of the measured noise, computed by sampling 100 synthetic Dopplergrams—generated with a unique source function on models with no background flows (Stejko et al. 2021b). This noise can be removed from our travel-time difference measurements (shown in Figure 3), by subtracting the corresponding noise profile initiated with the same source function (S; Equation (2)).

It is immediately evident that the helioseismic response is quite a bit weaker at all latitudinal averages when compared to travel-time differences measured from solar observations (see Section 5). The signal for model M5 (panel (b) of Figure 3) consistently hovers near zero at all depth ranges, with the slightest increase in strength at the 10°–30° range, coinciding with the development of strong rotational-axis aligned meridional circulation (Warnecke & Käpylä 2020). These flows are unable to form cohesive latitudinal cells, with the polar surface flows constantly switching directions as strong columnar convective cells penetrate from the interior. It becomes apparent that the quick succession of flow reversals associated with such multicell structures negates average helioseismic responses very rapidly with depth. It becomes difficult to distinguish an extremely weak global meridional flow, from a very strong one with near-surface reversals, as we move deeper into the convection zone. Another peculiar feature we observe is an oscillatory pattern of the signal with depth, seen clearly in model M5 and very slightly in model R1x. It appears that one of the hallmarks of a strong columnar multicell arrangement of the meridional flow can be rapid increases/decreases in travel-time differences that move between positive and negative values for the same latitudinal range. These reversals are smaller than the level of noise seen in observations, making them difficult to detect; however, they demonstrate a potential signature of a strong, rotationally constrained, multicell meridional flow. Model R1x shows a similar signal, however, with a stronger response in the 10°–30° latitudinal range. While the columnar convection deeper in the model interior appears similar to model M5, the poleward meridional flow on the solar surface is more continuous, possibly due to the lower rotational velocity of the model. This results in a measurably stronger signal in this range. This effect is even more pronounced in model H38 where a continuous surface latitudinal cell is allowed to form in the 10°–30° range; however, it is difficult to compare these two signals directly as

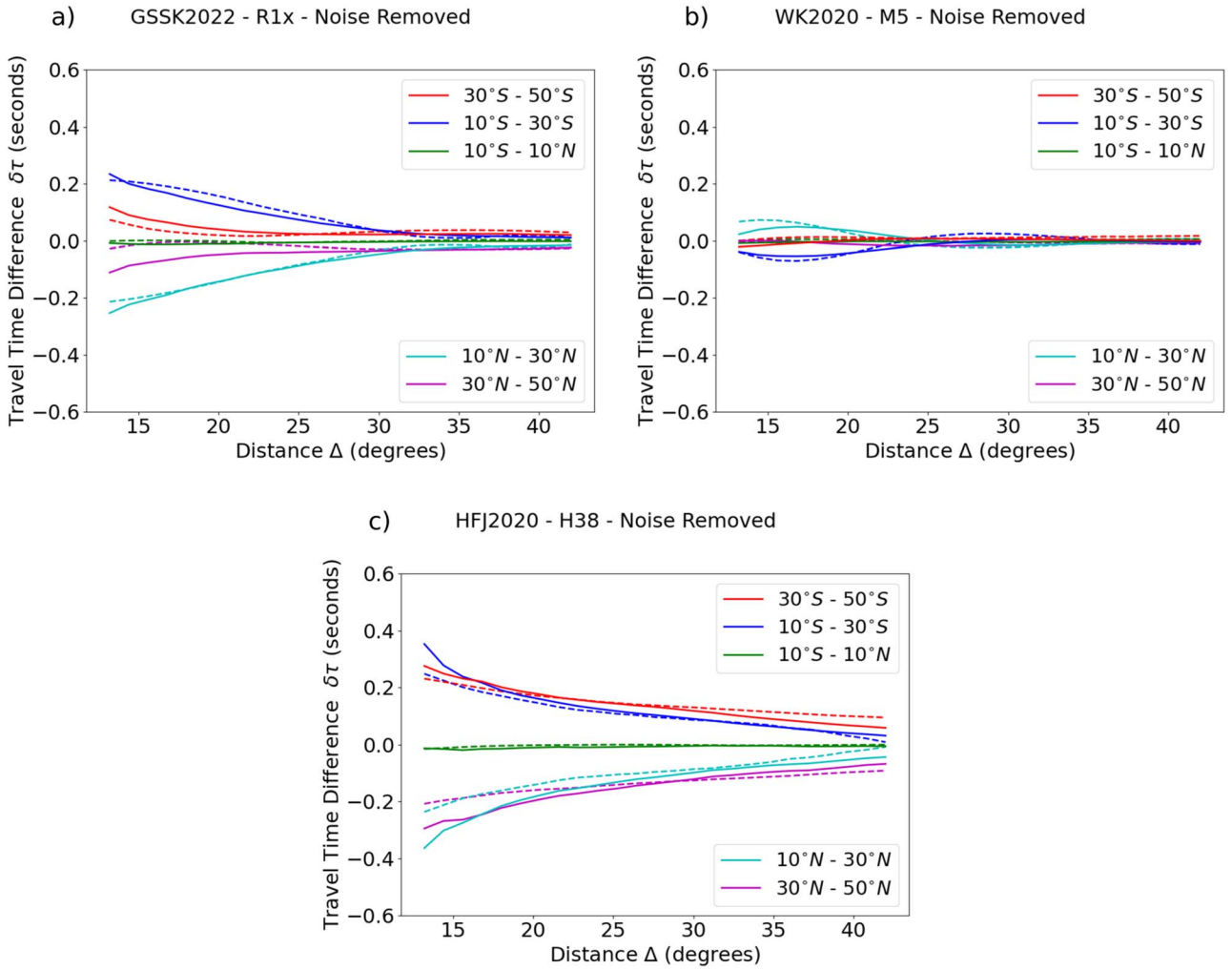

Figure 3. The N–S travel-time differences ($\delta\tau_{\rm NS}$) as a function of travel distance (Δ) for models R1x (a), M5 (b), and H38 (c). The travel-time measurements are phase-speed filtered ($\sigma = 0.05v_p$; Nigam et al. 2007), with profiles of noise subtracted and shown as solid lines for five latitudinal averages. Dashed lines are theoretical times computed using the ray-path approximation (Equation (4); Giles 2000).

the scaling of the average surface flow strength is very different in the two models ($\sim$10 m s^{-1} for model R1x, and $\sim$17 m s^{-1} for model H38). Even though the surface flow cell is stronger and more cohesive in model H38, the travel-time signal is not significantly stronger than in model R1x, as a near-surface return flow quickly negates its impact as we probe deeper into the interior. Model H38 is also characterized by a significant difference at higher latitudes, allowing strong (mostly) poleward flows to form throughout the entire extent of the model surface. This feature appears to be unique to the minimally rotationally constrained model, even among the other simulations of Hindman et al. (2020).

These models demonstrate that the strongest helioseismic responses are seen in regions where large continuous poleward flows are allowed to form on the surface and penetrate deeper into the model interior. While the arrangement of internal convective cells do show unique signals, their helioseismic responses may be indistinguishable within the noise of the lower half of the SCZ ($r < 0.85R_\odot$). Helioseismic constraints may not be able to tell us exactly how many circulation cells there are or their specific arrangement. These results, however, demonstrate that a strong baseline for surface flow speeds, combined with a drop-off in travel-time differences with depth, results in a good indication of whether a strong cohesive polar flow extends deep into the solar interior, as well as how likely a possible near-surface return flow is—as seen in the global helioseismic analysis of Mitra-Kraev & Thompson (2007) and the correlation tracking done by Hathaway (2012). We explore this question in greater detail in the next two sections by analyzing the effect of a changing return flow height on the helioseismic signal.

4. Analysis of Models with Varying Stratification Regimes

The effect of model stratification on the observed helioseismic signature is illustrated by comparing the two models of Matilsky et al. (2019) (N3 and N5), generated by the Rayleigh code. The meridional circulation profiles of these models can be seen in Figure 4, where, as in the previous section, the profiles are stretched to the solar surface ($R_\odot$). The models are actuated with identical input parameters, with the exception of the number of density scale heights; $N_\rho = 3$ for model N3 and $N_\rho = 5$ for model N5, resulting in bulk Rossby numbers of Ro $= 0.1345$ and Ro $= 0.4793$, respectively, for a rotation rate of $\Omega_0 = 2.7\Omega_\odot$ ($\Omega_0 = 3\Omega_\odot$ in their paper, where $\Omega_\odot = 2.6 \times 10^{-6}$ s^{-1}). An analysis of the local Rossby numbers (defined as Ro $= v'_{rms}(r)(2\Omega_0 H_\rho(r))^{-1}$, where $v'_{rms}(r)$ is a spherically averaged rms velocity and $H_\rho(r)$ is

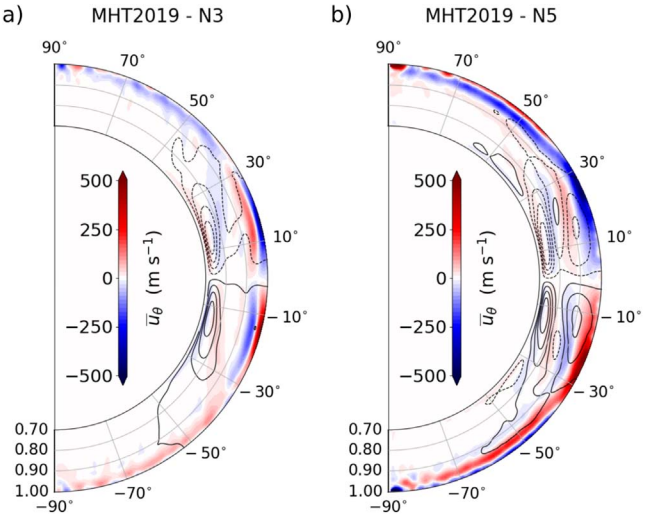

Figure 4. Latitudinal velocities ($\tilde{u}_\theta$) amplified to a maximum of 500 m s^{-1}. Meridional circulation profiles are generated by the Rayleigh code (Matilsky et al. 2019), contrasting models with (a) three density scale heights (N3) and (b) five density scale heights (N5). Solid and dashed contours represent counterclockwise and clockwise circulation, respectively, with positive (negative) values depicting a southward (northward) flow.

the local density scale height) by Matilsky et al. (2019) shows that the increased near-surface stratification in model N5 results in a rotationally unconstrained layer above $r/r_o \sim 0.97$, where $r_o = 6.586 \times 10^{10}$ cm, in their model, and corresponds to the solar radius ($r_o = R_\odot$) after we stretch it. Angular momentum transport in this region is dominated by inwardly directed turbulent Reynolds stresses resulting from the increased convective transport of downflow plumes. The impact of angular momentum transport due to columnar convection (Busse columns) is limited to rotationally constrained convection in the interior, allowing for the development of a larger more continuous global meridional flow cell near the surface of model N5.

We analyze the resulting helioseismic signatures by plotting the same latitudinal travel-time differences as in Section 3—corresponding to the approximate extent of continuous latitudinal features in the profiles. Figure 5 shows these latitudinal averages with the profile of noise removed for clarity. Solid lines correspond to the measured signal, while dashed lines are computed using the ray-path approximation (Equation (4); Giles 2000). The enlarged primary surface meridional flow cell in model N5 shows a significantly increased helioseismic response as compared to model N3, as well as the other solar convection models (R1x, M5, and H38). This is most pronounced at the 10°–30° latitude that shows almost a three-fold increase in average travel-time differences ($\delta\tau_{\rm NS}$) near the model surface. Higher latitudes ($>|30°|$) show a significantly diminished response due to the development of a reverse flow near the upper boundary of model N5. This reversal corresponds to a meridional torque attempting to balance the inward transport of angular momentum due to the Reynolds stresses in the region (Matilsky et al. 2019). The resulting equatorward surface flow at higher latitudes deviates from solar observations, requiring an as of yet unknown mechanism to balance it, and showing the need for a greater understanding of solar meridional flow structure.

Focusing on the 10°–30° latitudinal range shows that the presence of a large continuous poleward motion penetrating deeper into the model interior results in the most impactful change to the helioseismic signal, far outweighing the importance of any arrangement within the deep convective interior ($r < 0.90R_\odot$), whether that be the columnar multicell formations seen in models R1x/M5, or the less rotational-axis aligned multicell meridional circulation of models H38/N3. This inference is supported by results of previous works—showing that a double-cell meridional circulation profile, induced by a reversal near the base of the SCZ, shows slight differences when compared to a single-cell profile generated by the same mean-field solar model (Stejko et al. 2021b). A positive implication of these results is that, even though the internal arrangement of global flows may be inaccessible, results of local time–distance helioseismology can be effectively used to put constraints on the height of the initial flow reversal. We attempt to do this in the subsequent section by comparing the results of our helioseismic analysis with solar observations.

5. Comparison with Helioseismic Observations

In order to compare the results of our analysis directly to solar observations, we use the latest data from approximately

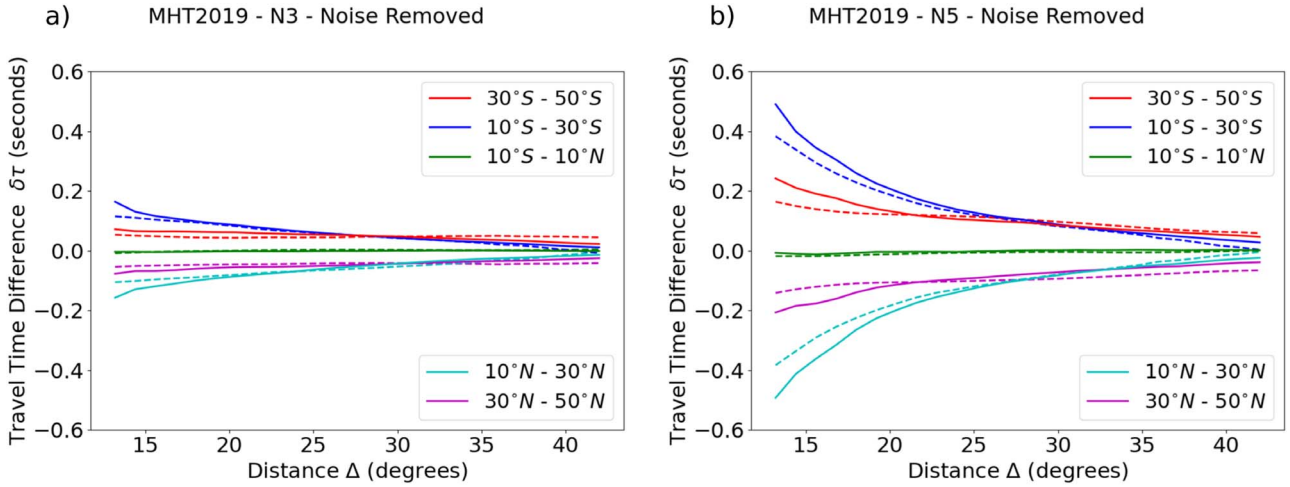

Figure 5. The N–S travel-time differences ($\delta\tau_{\rm NS}$) as a function of travel distance (Δ) for models N3 (a) and N5 (b). The travel-time measurements are shown under a phase-speed filter ($\sigma = 0.05v_p$; Nigam et al. 2007), with profiles of noise subtracted and shown as solid lines for five latitudinal averages. Dashed lines are theoretical times computed using the ray-path approximation (Equation (4); Giles 2000).

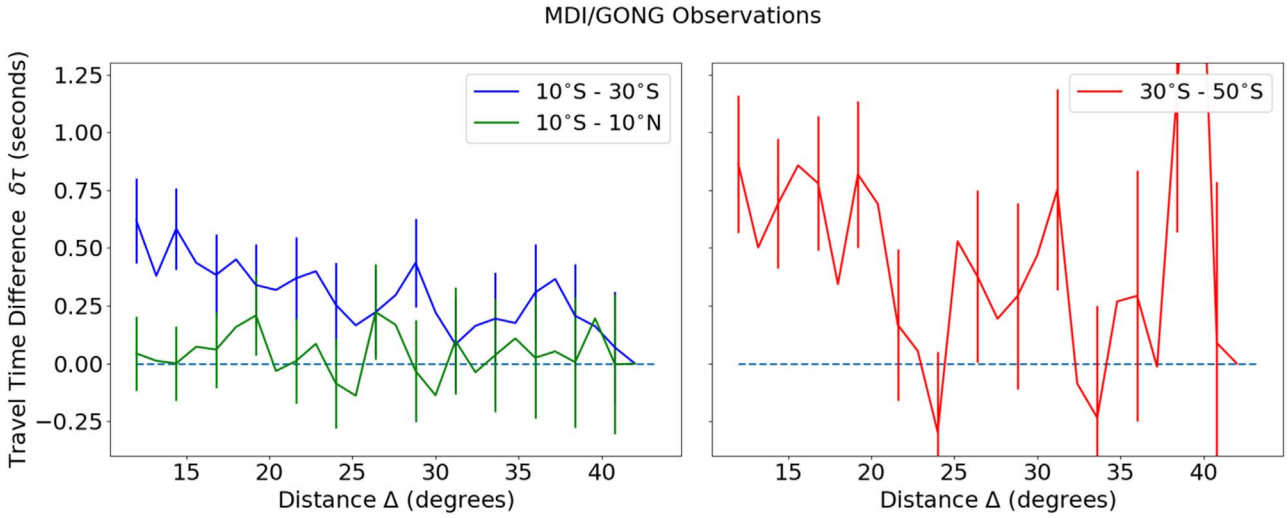

Figure 6. The N–S travel-time differences ($\delta\tau_{\rm NS}$) as a function of travel distance (Δ) for MDI/GONG data published by Gizon et al. (2020). Three latitude ranges are shown: 10°S–10°N, 10°S–30°S, and 30°S–50°S, averaged with their antisymmetric counterparts in the northern hemisphere in order to reduce noise, and plotted separately for clarity. Error bars are computed as the standard deviation (σ_{MG}; Equation (5)) of the travel-time differences in the 10°N–10°S latitude range from zero, scaled with the estimated noise for each measurement (see Gizon et al. 2020, supplementary materials).

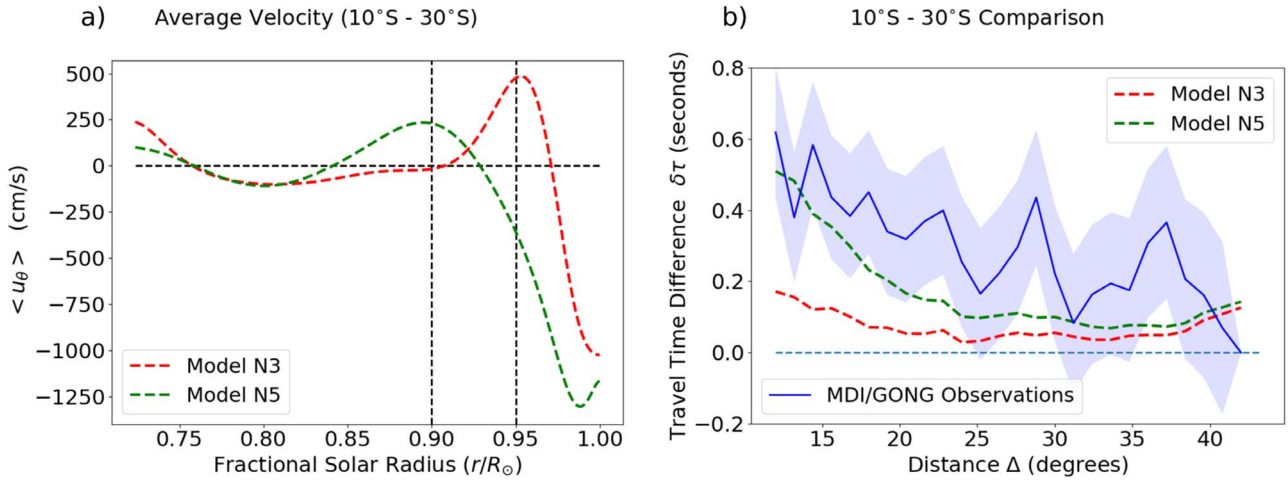

Figure 7. (a) The average latitudinal velocity $\langle u_\theta \rangle$ in the 10°S–30°S latitude range for models N3 (red) and N5 (green), stretched to the solar surface ($R_\odot$). (b) The N–S travel-time differences ($\delta\tau_{\rm NS}$) as a function of travel distance (Δ) for MDI/GONG data published by Gizon et al. (2020). Latitude ranges in both hemispheres are averaged in order to reduce noise and are compared to dashed lines representing latitudinal averages for models N3 (red) and N5 (green). The error range (blue region) is computed as the standard deviation (σ_{MG}; Equation (5)) of the travel-time differences in the 10°N–10°S latitude range from zero.

23 yr of combined observations made by the Michelson Doppler Imager (MDI; Scherrer et al. 1995) of the Solar and Heliospheric Observatory (SOHO), as well as the Global Oscillation Network Group (GONG; Harvey et al. 1996). The observations are described in detail and published by Gizon et al. (2020), publicly available at the Open Research Data Repository of the Max Planck Society. We show travel-time differences (Figure 6) for the same latitudinal averages as in our previous analyses. In order to reduce noise, we average the signals in both hemispheres, only showing 10°S–10°N, 10°S–30°S, and 30°S–50°S, and apply the same smoothing procedure used for our synthetic measurements (see Stejko et al. 2021b for details).

The noise at higher latitude ranges (30°S–50°S) is too high to make significant pronouncements—especially at greater depths ($\Delta > 20°$, $r < 0.87R_\odot$); however, the near-surface regions do show a signal more consistent with a continuous circulation cell (model H38) as opposed to the significant weakening/reversals seen in most of the other convectively driven models (R1x, M5, N3, and N5; Figures 3 and 5). We concentrate further analysis on the 10°S–30°S latitudinal range where noise is significantly reduced. The average latitudinal velocity in this range ($\langle u_\theta \rangle$) is shown in panel (a) of Figure 7 for models N3 and N5. The deep return flow cell structure (N5) begins to diverge from the shallow one (N3) at approximately $r = 0.80R_\odot$, showing the structure of two potential return flow profiles that culminate in an average surface velocity of approximately 10 m s^{-1}, with a maximum of 20 m s^{-1}. In panel (b) of Figure 7 we show the travel-time differences computed from synthetic Dopplergrams (dashed lines) for models N3 and N5 (see Figure 5) in this region, comparing them to MDI/GONG observations (Gizon et al. 2020; solid line) in the same latitudinal range. The error bars are computed as one standard deviation (Equation (5)) of the travel-time differences in the 10°N–10°S latitude range from zero, scaled with the estimated noise (see Gizon et al. 2020, supplementary materials) for each travel-time difference measurement as a function of travel

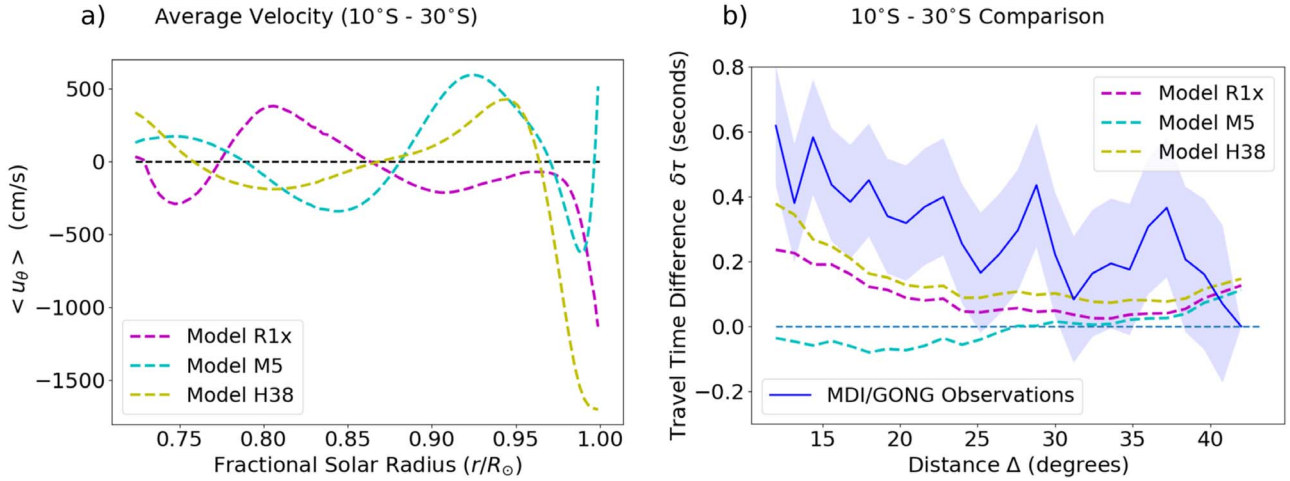

Figure 8. (a) The average latitudinal velocity $\langle u_\theta \rangle$ in the 10°S–30°S latitude range for models R1x (magenta), M5 (cyan), and H38 (yellow), stretched to the solar surface ($R_\odot$). (b) The N–S travel-time differences ($\delta\tau_{\rm NS}$) as a function of travel distance (Δ) for MDI/GONG data published by Gizon et al. (2020). Latitude ranges in both hemispheres are averaged in order to reduce noise and are compared to dashed lines representing latitudinal averages for models R1x (magenta), M5 (cyan), and H38 (yellow). The error range (blue region) is computed as the standard deviation (σ_{MG}; Equation (5)) of the travel-time differences in the 10°N–10°S latitude range from zero.

distance (Δ) and latitude:

$$\sigma_{MG} = \sqrt{\frac{1}{N}\sum_{i=1}^{N}\delta\tau_i^2}. \quad (5)$$

The travel-time differences calculated for model N5 are a better match for the observational signal at depths $r > 0.80R_\odot$. The average z-score (number of standard deviations from the mean) of the signal in this depth range is $z_{N5} = 0.803$ for model N5, and $z_{N3} = 1.598$ for model N3. Assuming that the travel-time difference measurements of models N3 and N5 are the mean of a normal noise distribution with a standard deviation of σ_{MG}, the probability of measuring a signal at least as extreme (p-value) as the travel-time differences computed by Gizon et al. (2020) (10°S–30°S, $12 < \Delta < 30°$) would be approximately $p_{N3} = 0.055$ for model N3 and $p_{N5} = 0.21$ for model N5—representing a significantly increased likelihood that the average depth of the maximum return flow in this latitude range is approximately at or slightly below $r \sim 0.90R_\odot$, assuming an accurate scaling of surface flows ($10\,{\rm m\,s^{-1}}$ average with a $20\,{\rm m\,s^{-1}}$ maximum; see Roudier et al. 2018).

A similar comparison of models R1x, M5, and H38 to solar observational data from MDI/GONG can be seen in panel (b) of Figure 8; however, as shown by the average velocities in the 10°S–30°S latitudinal range in panel (a), the surface flow scaling of all three simulations are radically different from each other. Model R1x is the only simulation that has an average surface velocity of $\sim 10\,{\rm m\,s^{-1}}$; as such, we compute its p-value to be $p_{R1x} = 0.079$—slightly above that of model N3. Model M5 exhibits travel-time differences close to zero, which comports with an average velocity in this latitudinal range that is not particularly strong (Figure 8)—due to the averaging of several reversals penetrating to the surface in this range. Model H38 seems to be within one standard deviation of solar observations; however, this is most likely because the maximum surface velocity ($20\,{\rm m\,s^{-1}}$) is more sustained in the 10°S–30°S latitudinal range of model H38, resulting in an average surface velocity of $\sim 17\,{\rm m\,s^{-1}}$. This is most likely the result of a smaller bulk rotational constraint on the flows of model H38, which has a rotation rate of $2\Omega_\odot$ as opposed to the faster rotation ($2.7\Omega_\odot$) seen in models N3 and N5. This appears to allow for the development of a stronger surface cell; however, since the surface scaling of the average velocity is significantly increased, it is difficult to compare with models N3 and N5 directly.

The three different implementations of convectively driven global solar simulations that we analyze generate meridional circulation profiles that are quite distinct, and while they can give us general insights, they can be difficult to compare quantitatively. In order to draw meaningful conclusions from a comparison of simulation results to solar observations, we focus our analysis on the three models whose average surface velocities are the same in our region of interest ($\sim 10\,{\rm m\,s^{-1}}$ in 10°S–30°S): models R1x, N3, and N5. The major differentiating factor in these models is in the depth of the primary circulation cell on the model surface. Whether the arrangement is a strong columnar multicell structure, such as in model R1x, or a more latitudinal one with weaker columnar cells, as in model N3, they exhibit minimal travel-time differences—showing a very small drop-off with depth. The addition of realization noise leaves the signals appearing nearly horizontal (see Figure 2). A comparison with solar observations shows that this is unlikely to be the case, as measured travel-time differences show a very distinct slope, larger than the error associated with the measurement (Figure 6). We show that such a slope is most strongly associated with the radial extent of the primary circulation cell, corresponding to a minimal depth of the maximum return flow at $\sim 0.90R_\odot$. This result, however, is strongly dependent on the proper estimate of meridional flow strength on the solar surface, which is variable, requires long temporal sampling windows to accurately gauge (Hathaway 1996; Ulrich 2010; Kosovichev & Zhao 2016; Roudier et al. 2018), and becomes unreliable at higher latitudes (±45°) owing to projection effects such as foreshortening.

6. Discussion

Global convectively driven hydrodynamic models are unlikely to be able to recreate the conditions of the solar interior any time soon. The extreme dynamics of turbulent solar

convection—with dimensional parameter estimates of a Reynolds number in the range of Re$\sim 10^{10}$–10^{13} and a Rayleigh number of Ra $\sim 10^{20}$ (see Rincon 2006)—preclude a full understanding of the organization of buoyant injection and turbulent dissipation in the large range of turbulent scales. This leaves us with a necessity of estimating the action of subgrid-scale turbulent dissipation with techniques such as the large eddy simulation (LES) implementation of the dynamic Smagorinsky model (Germano et al. 1991). Other techniques to simulate the dissipation rate and the cascade of energy in the inertial subrange use implicit methods (e.g., "implicit" large eddy simulation, or ILES; Grinstein et al. 2007), which simulate turbulent dissipation via a truncation of high-order terms in the computational scheme. While such methods have found success in replicating the organization of turbulence in direct numerical simulations (DNSs; Elliott & Smolarkiewicz 2002), it is difficult to gauge if they are a realistic proxy for the solar interior. This is especially true considering the high stratification of solar plasma and the large range of energetic scales. This becomes a greater concern near the solar surface, along with an increasing velocity, compression, and radiation effects that are too computationally expensive to model. This can be problematic for numerical simulations, as it is becoming increasingly apparent that these upper layers may be necessary in order to fully replicate global solar dynamics (Stejko et al. 2020).

Even though global modeling has its limitations, it remains a useful tool for understanding the actions of chaotic systems within defined parameters. Rather than trying to simulate exact solar conditions, parameters can be tweaked to create a more robust understanding of the set of conditions that result in dynamical behaviors observed on the Sun. In hydrodynamic regimes this means reproducing global mean flow patterns such as differential rotation and meridional circulation. To that end we demonstrate how forward-modeling the helioseismic inferences of meridional circulation can be used as an additional constraint on global MHD/HD models, and improve our understanding of the convective turbulent parameters and stratification profiles needed to more accurately simulate solar conditions. We show that the multicell arrangement commonly associated with convection simulations that reproduce solar-like differential rotation (e.g., Guerrero et al. 2013; Käpylä et al. 2013; Fan & Fang 2014; Warnecke & Käpylä 2020; Hotta et al. 2022) exhibits a weak travel-time difference signal with a strong curvature that can oscillate around zero with increasing depth. This signal seems to be characteristic of the development of rotationally constrained columnar convection at low latitudes. A more linear drop-off curve is seen in models that develop more latitudinal flows near the surface, with weaker internal columnar convection (H38 and N3); however, they still show a small helioseismic response. Increasing the radial extent of the primary circulation cell at the model surface causes the most pronounced impact, allowing convective models (N5) to most closely replicate solar observations. This impact is greater than one standard deviation of the realization noise, making it an effective constraint on mean meridional flows generated by MHD/HD models. While these models are far from accurate simulations of solar dynamics, understanding the character of their global mean mass-flows can point us in the direction of more realistic solar simulations. Extending 3D global simulations to the solar surface is currently computationally unfeasible; however, this analysis reinforces the idea that the increased density stratification in near-surface layers may be necessary to adequately replicate global solar processes.

A.M.S. would like to thank the heliophysics modeling and simulation team at NASA Ames Research Center for their support. This work is supported by the NASA grants 80NSSC19K0630, 80NSSC19K1436, NNX14AB70G, NNX17AE76A, 80NSSC20K0602, 80NSSC17K0008, 80NSSC18K1125, 80NSSC19K0267, 80NSSC20K0193, 80NSSC19K1428, NNX13AG18G, NNX16AC92G, NNX17AG22G, 80NSSC18K1127. J.W. acknowledges funding by the European Research Council (ERC) under the European Union's Horizon 2020 research and innovation program (grant agreement No. 818665 "UniSDyn"). The authors thank the NASA Drive Science Center studying the Consequences Of Fields and Flows in the Interior and Exterior of the Sun (COFFIES) for providing multidisciplinary collaboration opportunities in heliophysics.

Facility: NASA AMES (NAS HECC).

Software: GALE (Stejko et al. 2021b), EULAG-MHD (Smolarkiewicz & Charbonneau 2013), Rayleigh code (https://github.com/geodynamics/Rayleigh); Featherstone et al. 2021; Featherstone & Hindman 2016), Pencil code (https://github.com/pencil-code/pencil-code; Pencil Code Collaboration et al. 2021).

ORCID iDs

Andrey M. Stejko https://orcid.org/0000-0001-7483-3257
Alexander G. Kosovichev https://orcid.org/0000-0003-0364-4883
Nicholas A. Featherstone https://orcid.org/0000-0002-2256-5884
Gustavo Guerrero https://orcid.org/0000-0002-2671-8796
Bradley W. Hindman https://orcid.org/0000-0001-7612-6628
Loren I. Matilsky https://orcid.org/0000-0001-9001-6118
Jörn Warnecke https://orcid.org/0000-0002-9292-4600

References

Birch, A. C., & Kosovichev, A. G. 2001, in ESA SP-464, SOHO 10/GONG 2000 Workshop: Helio- and Asteroseismology at the Dawn of the Millennium, ed. A. Wilson & P. L. Pallé (Noordwijk: ESA), 187
Braun, D. C., & Birch, A. C. 2008, ApJL, 689, L161
Busse, F. H. 1970, ApJ, 159, 629
Charbonneau, P. 2020, LRSP, 17, 4
Chen, R. 2019, PhD thesis, Stanford Univ.
Christensen-Dalsgaard, J., Dappen, W., Ajukov, S. V., et al. 1996, Sci, 272, 1286
Elliott, J. R., & Smolarkiewicz, P. K. 2002, IJNMF, 39, 855
Fan, Y., & Fang, F. 2014, ApJ, 789, 35
Featherstone, N. A., Edelmann, P. V. F., Gassmoeller, R., et al. 2021, geodynamics/Rayleigh: Rayleigh v1.0.1, Zenodo, doi: 10.5281/zenodo.5774039
Featherstone, N. A., & Hindman, B. W. 2016, ApJ, 818, 32
Featherstone, N. A., & Miesch, M. S. 2015, ApJ, 804, 67
Gastine, T., Yadav, R. K., Morin, J., Reiners, A., & Wicht, J. 2014, MNRAS, 438, L76
Germano, M., Piomelli, U., Moin, P., & Cabot, W. H. 1991, PhFl, 3, 1760
Giles, P. M. 2000, PhD thesis, Stanford Univ.
Gilman, P. A. 1972, SoPh, 27, 3
Gilman, P. A., & Miller, J. 1981, ApJS, 46, 211
Gizon, L., Cameron, R. H., Pourabdian, M., et al. 2020, Sci, 368, 1469
Grinstein, F. F., Margolin, L. G., & Rider, W. J. 2007, Implicit Large Eddy Simulation: Computing Turbulent Fluid Dynamics (Cambridge: Cambridge Univ. Press),

Guerrero, G., Smolarkiewicz, P. K., Kosovichev, A. G., & Mansour, N. N. 2013, ApJ, 779, 176
Hartlep, T., Zhao, J., Kosovichev, A. G., & Mansour, N. N. 2013, ApJ, 762, 132
Harvey, J. W., Hill, F., Hubbard, R. P., et al. 1996, Sci, 272, 1284
Hathaway, D. H. 1996, ApJ, 460, 1027
Hathaway, D. H. 2012, ApJ, 760, 84
Hindman, B. W., Featherstone, N. A., & Julien, K. 2020, ApJ, 898, 120
Hotta, H., Kusano, K., & Shimada, R. 2022, ApJ, 933, 199
Howe, R., Larson, T. P., Schou, J., et al. 2011, JPhCS, 271, 012061
Käpylä, P. J., Mantere, M. J., & Brandenburg, A. 2012, ApJL, 755, L22
Käpylä, P. J., Mantere, M. J., Cole, E., Warnecke, J., & Brandenburg, A. 2013, ApJ, 778, 41
Käpylä, P. J., Mantere, M. J., Guerrero, G., Brandenburg, A., & Chatterjee, P. 2011, A&A, 531, A162
Kholikov, S., Serebryanskiy, A., & Jackiewicz, J. 2014, ApJ, 784, 145
Kitchatinov, L. L. 2004, ARep, 48, 153
Kitchatinov, L. L., & Ruediger, G. 1995, A&A, 299, 446
Kosovichev, A. G., & Duvall, T. L. 1997, in SCORe'96 : Solar Convection and Oscillations and their Relationship, Astrophysics and Space Science Library, Vol. 225, ed. F. P. Pijpers, J. Christensen-Dalsgaard, & C. S. Rosenthal (Dordrecht: Kluwer Academic), 241
Kosovichev, A. G., & Zhao, J. 2016, in Lecture Notes in Physics, Vol. 914 ed. J.-P. Rozelot & C. Neiner (Berlin: Springer), 25
Kosovichev, A. G., Schou, J., Scherrer, P. H., et al. 1997, SoPh, 170, 43
Liang, Z.-C., & Chou, D.-Y. 2015, ApJ, 805, 165
Lin, C.-H., & Chou, D.-Y. 2018, ApJ, 860, 48
Matilsky, L. I., Hindman, B. W., & Toomre, J. 2019, ApJ, 871, 217
Matilsky, L. I., Hindman, B. W., & Toomre, J. 2020, ApJ, 898, 111
Mitra-Kraev, U., & Thompson, M. J. 2007, AN, 328, 1009
Nigam, R., Kosovichev, A. G., & Scherrer, P. H. 2007, ApJ, 659, 1736
Pencil Code Collaboration, Brandenburg, A., Johansen, A., et al. 2021, JOSS, 6, 2807
Pipin, V. V., & Kosovichev, A. G. 2018, ApJ, 854, 67
Rajaguru, S. P., & Antia, H. M. 2020, in Dynamics of the Sun and Stars; Honoring the Life and Work of Michael J. Thompson, ed. M. J. P. F. G. Monteiro et al. (Cham: Springer), 107
Rempel, M. 2005, ApJ, 622, 1320
Rincon, F. 2006, JFM, 563, 43
Roudier, T., Švanda, M., Ballot, J., Malherbe, J. M., & Rieutord, M. 2018, A&A, 611, A92
Ruediger, G. 1989, Differential Rotation and Stellar Convection. Sun and the Solar Stars (Berlin: Akademie)
Schad, A., Timmer, J., & Roth, M. 2013, ApJL, 778, L38
Scherrer, P. H., Bogart, R. S., Bush, R. I., et al. 1995, SoPh, 162, 129
Schou, J., Antia, H. M., Basu, S., et al. 1998, ApJ, 505, 390
Schou, J., Howe, R., Basu, S., et al. 2002, ApJ, 567, 1234
Smolarkiewicz, P. K., & Charbonneau, P. 2013, JCoPh, 236, 608
Stejko, A. M., Guerrero, G., Kosovichev, A. G., & Smolarkiewicz, P. K. 2020, ApJ, 888, 16
Stejko, A. M., Kosovichev, A. G., & Mansour, N. N. 2021a, ApJS, 253, 9
Stejko, A. M., Kosovichev, A. G., & Pipin, V. V. 2021b, ApJ, 911, 90
Ulrich, R. K. 2010, ApJ, 725, 658
Warnecke, J. 2018, A&A, 616, A72
Warnecke, J., & Käpylä, M. J. 2020, A&A, 642, A66
Zhao, J., Bogart, R. S., Kosovichev, A. G., Duvall, T. L., & Hartlep, T, J. 2013, ApJL, 774, L29
Zhao, J., Hartlep, T., Kosovichev, A. G., & Mansour, N. N. 2009, ApJ, 702, 1150
Zhao, J., Nagashima, K., Bogart, R. S., Kosovichev, A. G., & Duvall, T. L. 2012, ApJL, 749, L5